Penalized-Likelihood Reconstruction with High-Fidelity Measurement Models for High-Resolution Cone-Beam Imaging

Steven Tilley II, **Matthew Jacobson**, **Qian Cao**, **Michael Brehler**, **Alejandro Sisniega**, **Wojciech Zbijewski**, and **J. Webster Stayman [Senior Member, IEEE]**

Department of Biomedical Engineering, Johns Hopkins University

Abstract

We present a novel reconstruction algorithm based on a general cone-beam CT forward model which is capable of incorporating the blur and noise correlations that are exhibited in flat-panel CBCT measurement data. Specifically, the proposed model may include scintillator blur, focal-spot blur, and noise correlations due to light spread in the scintillator. The proposed algorithm (GPL-BC) uses a Gaussian Penalized-Likelihood objective function which incorporates models of Blur and Correlated noise. In a simulation study, GPL-BC was able to achieve lower bias as compared to deblurring followed by FDK as well as a model-based reconstruction method without integration of measurement blur. In the same study, GPL-BC was able to achieve better line-pair reconstructions (in terms of segmented-image accuracy) as compared to deblurring followed by FDK, a model based method without blur, and a model based method with blur but not noise correlations. A prototype extremities quantitative cone-beam CT test bench was used to image a physical sample of human trabecular bone. These data were used to compare reconstructions using the proposed method and model based methods without blur and/or correlation to a registered μCT image of the same bone sample. The GPL-BC reconstructions resulted in more accurate trabecular bone segmentation. Multiple trabecular bone metrics, including Trabecular Thickness (Tb.Th.) were computed for each reconstruction approach as well as the μCT volume. The GPL-BC reconstruction provided the most accurate Tb.Th. measurement, 0.255 mm, as compared to the μCT derived value of 0.193 mm, followed by the GPL-B reconstruction, the GPL-I reconstruction, and then the FDK reconstruction (0.271 mm, 0.309 mm, and 0.335 mm, respectively).

Index Terms

Model-based Iterative Reconstruction; Deconvolution; Noise Correlation; Trabecular Bone; Extremities Imaging

I. Introduction

Flat-panel-based cone-beam CT (CBCT) has offered more compact systems and improved spatial resolution as compared to multirow detector CT (MDCT). These advantages have resulted in prototype and commercial CBCT systems for specific applications, such as mammography [1], [2] and extremities imaging [3], [4], where high spatial resolution is critical. For example in mammography, clinicians would like to detect and visualize small

microcalcifications of <100 μm [5]. In extremities imaging, analysis of trabecular bone morphology for quantitative assessment is desired with trabecular detail of 50–150 μm [6]. The spatial resolution requirements for these tasks often lie just beyond current system capabilities (~180–350 μm [7], [8] for commercial systems). Thus, even a modest improvement in spatial resolution has the potential to dramatically improve the clinical utility of CBCT systems.

Model-based iterative reconstruction (MBIR) techniques have been shown to improve image quality in multi-detector CT (MDCT) [9] as compared to analytical approaches such as FDK [10]. Much of the advantage of MBIR methods derives from the inclusion of a high-fidelity forward model containing both a model of the physical acquisition process and a mathematical formulation of measurement statistics. For example, the noise model informs the reconstruction algorithm about the relative information content of different measurements, allowing weights on the relative importance of these measurements in reconstructing the image.

While MBIR methods have been successfully applied to CBCT [11]–[13], the system models are often borrowed directly from MDCT, and are therefore derived from assumptions that may not be valid for CBCT. For example, MDCT detectors typically include mechanisms to avoid signal sharing between detector elements (e.g., a pixelated scintillator) whereas flat-panel detectors typically exhibit significant sharing of the light generated by the primary x-ray to secondary light quanta conversion. This effect can be prominent for smaller pixel sizes and leads to increased blur and noise correlation between neighboring measurements as compared to MDCT. While previous work [14], [15] has suggested that focal spot modeling has relatively small advantages in current MDCT systems, the X-ray tubes used in many dedicated CBCT systems tend to have stationary anodes and larger focal spots than those used in MDCT. Additionally, CBCT detectors have smaller pixels than MDCT. Specifically, [15] demonstrated that focal spot modeling lead to improvements when the effective focal spot blur (at the detector) was about 1.3 detector elements wide, which is an uncommon occurrence in MDCT but common in CBCT (e.g., 0.2 mm pixels with a 0.3 mm focal spot and a system magnification of 2). Hence, focal spot blurring effects can be significant in CBCT, particularly in systems that leverage higher magnifications. Traditional MDCT methods do not incorporate such physical effects into their forward models, limiting their ability to resolve fine resolution details when applied to flat-panel CBCT data. To get the most of such data (e.g., increasing spatial resolution capabilities), the MBIR forward model must adopt high-fidelity models of these physical effects which are conventionally ignored.

Emission imaging has utilized high-fidelity modeling to recover lost spatial resolution for decades [16]–[21]. The linear forward model in SPECT and PET imaging permits incorporation of advanced blur models directly into the system matrix. The resulting high-fidelity forward models are linear, simplifying optimization. Such approaches have been used to model position-dependent geometric blurs and blurs due to physical detector characteristics (e.g., signal penetration through septa) [16]–[21]. Additionally, noise correlations induced by rebinning have been modeled for PET [22].

In contrast to emission imaging, transmission imaging forward models are fundamentally nonlinear due to the Beer-Lambert law, preventing blurs from simply being incorporated into the system matrix. Applications of advanced forward models in transmission tomography can be coarsely grouped into three categories: sinogram restoration, direct MBIR, and preprocessing + MBIR. In sinogram restoration approaches, ideal measurements or line integrals are estimated based on a forward model. Images are reconstructed from these estimates with either analytical methods (e.g., FDK) or MBIR with a simple forward model. Sinogram restoration has been used in conjunction with models of blur [23], [24] and noise correlation [25]. Direct MBIR methods incorporate the advanced forward models (e.g., of blur, noise correlation) directly into the MBIR objective function. Such approaches have been used with an independent noise assumption [26], [27]. Additionally, direct MBIR has been used to model blur and noise correlation in tomosynthesis [28] by assuming uniform quantum noise per view and that features of interest (e.g., microcalcifications) have low-attenuation and are small. Preprocessing + MBIR is a hybrid approach, with the effects of preprocessing modeled in the subsequent MBIR. For example, noise correlations induced by deblurring have been included in an MBIR model for CBCT [29].

Recently, we presented a novel preprocessing + MBIR method which can incorporate spatial blur and noise correlations in a linear penalized weighted least-squares framework [29]. This method demonstrates the importance of high fidelity system modeling, specifically regarding spatial noise correlation, but contained undesirable complexities due to the linearization of the forward model. Specifically, this linearized forward model operates on an estimation of the line integrals, requiring a preprocessing step that deconvolves system blurs prior to reconstruction. The deconvolution requires solving an inverse problem with tunable parameters such as regularization type and strength. To overcome this limitation, we have presented a direct MBIR method with a non-linear objective function and steepest-descent optimizer [30], which uses the measurement data directly to avoid the separate deblurring step and resulting regularization of [29].

In this work we present a novel direct MBIR method based on the non-linear least-squares forward model and objective function of [30] which may incorporate blur, noise correlation, and a Gaussian noise model for the measurements. The optimization algorithm utilizes optimization transfer and separable surrogates, similar to the algorithm in [31], [32]. We derive the algorithm for this Gaussian Penalized-Likelihood (PL) objective with modeled Blur and noise Correlation (GPL-BC), and evaluate performance relative to the same algorithm with simpler forward models. Specifically, GPL-I assumed there was no blur in the model (Identity blur), and GPL-B assumed no noise correlation. The GPL methods are compared to a Deblurring + FDK (dFDK) method, where measurement data are deblurred prior to FDK reconstruction. Blur measurements from a prototype extremities quantitative CBCT (qCBCT) test bench [4] were used to construct a simulation study measuring the image quality of reconstructed line-pairs. The qCBCT test bench was used to scan a sample of human trabecular bone. Reconstructions of the bone using FDK, GPL-I, GPL-B, and GPL-BC were compared to each other as well as a registered μCT scan of the same sample. Finally, quantitative metrics of Trabecular Thickness (Tb.Th.), Trabecular Spacing (Tb.Sp.), and Bone Volume to Total Volume (BV/TV) were calculated and evaluated for each approach [33]–[35].

II. Methods

A. Forward Model and Objective Function

A general high-fidelity forward model of the measurements may be expressed as

$$\bar{y}_i = \sum_k^{n_y} B_{ik} \exp \left(-\sum_j^{n_\mu} A_{kj}\mu_j \right) \quad (1)$$

where $\bar{y}_i$ is the expected value of measurement i and μ_j is the attenuation value of voxel j. We assume that the measurements are a sample of a multivariate Gaussian distribution with means given by (1) and covariance matrix $\mathbf{K}$. By representing the mean measurements as vector $\bar{\boldsymbol{y}}$, the attenuation values as vector $\boldsymbol{\mu}$, and the B and A terms as elements of matrices $\mathbf{B}$ and $\mathbf{A}$, respectively, the notation can be simplified as:

$$\bar{\boldsymbol{y}} = \mathbf{B}e^{-\mathbf{A}\boldsymbol{\mu}} \quad (2a)$$

$$\boldsymbol{y} \sim \mathcal{N}(\bar{\boldsymbol{y}}, \mathbf{K}) \quad (2b)$$

where (2a) is the mean forward model and (2b) is the noise model. ($\mathcal{N}$ indicates a normal distribution, in this case with a mean of $\bar{\boldsymbol{y}}$ and covariance matrix $\mathbf{K}$.) With this notation the exponential function is applied element-wise. Throughout, matrix and vector variables are boldfaced, and variables indicating elements of these matrices and vectors are not bold, and have a subscript indicating which element they refer to (e.g., y_i is the ith element of $\boldsymbol{y}$ and B_{ik} is the element at the ith row and kth column of $\mathbf{B}$). Traditionally, $\mathbf{A}$ is the forward projector, $\mathbf{B}$ is a diagonal matrix that scales raw transmission values based on the photon fluence associated with each measurement, and $\mathbf{K}$ is a diagonal matrix of the measurement variances (i.e., the covariance matrix with an independent noise model). While these are conventional choices in the forward model, (2) is sufficiently general to accommodate more complex physical characteristics including system blurs (if $\mathbf{B}$ is a blurring matrix) and correlated noise (if $\mathbf{K}$ is a non-diagonal covariance matrix). In this work, we focus on modeling scintillator and focal-spot blur as part of $\mathbf{B}$, and noise correlation due to the scintillator blur in $\mathbf{K}$. Specifically, both blurs are modeled as shift-invariant convolutions. While this ignores focal-spot geometric effects (e.g., depth dependence) it is an appropriate approximation in many scenarios (e.g., thin objects, narrow fan angle). See Appendix D in the Supplementary Materials[1] for a derivation of the approximation. (Note that this approximation is not imposed by the forward model, which is capable of modeling shift-variance and depth dependence.)

---

[1]available in the supplementary files/multimedia tab

Algorithm 1

Algorithm to minimize (3). The number of iterations is given by P and the number of ordered subsets by M. The combined iteration and subset index is given by a fractional value, n. For Nesterov acceleration, use *both* initialization columns and the *right* update column. Otherwise, use the *left* initialization column and the *left* update column. Element-wise multiplication is denoted by the $\circ$ operator. The $[\cdot]_+$ operator returns the (element-wise) maximum of its argument and 0.

Common Initialization	AND	Nesterov Initialization
$\boldsymbol{\eta} \leftarrow \mathbf{B}^T\mathbf{W}\mathbf{B}\mathbf{1}$ $\boldsymbol{\gamma} \leftarrow \mathbf{A}\mathbf{1}$ Calculate $\mathbf{B}^T\mathbf{W}\boldsymbol{y}$		$\boldsymbol{z} \leftarrow \boldsymbol{\mu}^{(0)}$ $\boldsymbol{w} \leftarrow 0$ $t^{(0)} \leftarrow 1$ $t_{sum} \leftarrow t^{(0)}$

for $p \leftarrow 0..P-1$ **do**
    for $m \leftarrow 0..M-1$ **do**
        $n \leftarrow p + m/M, \quad \boldsymbol{l}^{(n)} \leftarrow \mathbf{A}_{(m)}\boldsymbol{\mu}^{(n)}, \quad \boldsymbol{x}^{(n)} \leftarrow \mathrm{e}^{-\boldsymbol{l}^{(n)}}$
        $\boldsymbol{\rho}^{(n)} \leftarrow [\mathbf{B}^T\mathbf{W}\mathbf{B}]_{(m)}\boldsymbol{x}^{(n)} - [\mathbf{B}^T\mathbf{W}\boldsymbol{y}]_{(m)} - \boldsymbol{\eta}_{(m)} \circ \boldsymbol{x}^{(n)}$
        $\boldsymbol{L}^{(n)} \leftarrow M\mathbf{A}_{(m)}^T[-\boldsymbol{\eta}_{(m)} \circ \boldsymbol{x}^{(n)} \circ \boldsymbol{x}^{(n)} - \boldsymbol{\rho}^{(n)} \circ \boldsymbol{x}^{(n)}]$

$$c_i^{(n)} = \begin{cases} \left[2\dfrac{0.5\eta_i + \rho_i^{(n)} - 0.5\eta_i(x_i^{(n)})^2 - x_i^{(n)}\rho_i^{(n)} - l_i^{(n)}\left(\eta_i(x_i^{(n)})^2 + \rho_i^{(n)}x_i^{(n)}\right)}{(l_i^{(n)})^2} \right]_+ & l_i^{(n)} > 0 \\[2ex] \left[2\eta_i + \rho_i^{(n)} \right]_+ & l_i^{(n)} = 0 \end{cases}$$

        $\boldsymbol{D}^{(n)} \leftarrow M\mathbf{A}_{(m)}^T\left(\boldsymbol{\gamma}_{(m)} \circ \boldsymbol{c}^{(n)}\right)$
        Calculate penalty surrogate gradient ($\triangledown\Phi^{(n)}$) and curvature ($\triangledown^2\Phi^{(n)}$)
        $\Delta\boldsymbol{\mu} \leftarrow \dfrac{\boldsymbol{L}^{(n)} + \triangledown\Phi^{(n)}}{\boldsymbol{D}^{(n)} + \triangledown^2\Phi^{(n)}}$

Normal Update	OR	Nesterov Update
$\boldsymbol{\mu}^{(n+1/M)} \leftarrow [\boldsymbol{\mu}^{(n)} - \Delta\boldsymbol{\mu}]_+$		$t^{(n+1/M)} \leftarrow \frac{1}{2}(1 + \sqrt{1 + 4(t^{(n)})^2})$, $t_{sum} \leftarrow t_{sum} + t^{(n+1/M)}, \quad \boldsymbol{z} \leftarrow [\boldsymbol{\mu}^{(n)} - \Delta\boldsymbol{\mu}]_+,$ $\boldsymbol{w} \leftarrow \boldsymbol{w} + t^{(n)}\Delta\boldsymbol{\mu}, \qquad \boldsymbol{v} \leftarrow [\boldsymbol{\mu}^{(0)} - \boldsymbol{w}]_+,$ $\boldsymbol{\mu}^{(n+1/M)} \leftarrow \boldsymbol{z} + t^{(n+1/M)}/t_{sum}(\boldsymbol{v} - \boldsymbol{z})$

    end for
end for

Equation 2 also assumes the measurements have an underlying Gaussian distribution. The PL objective function resulting from (2) is therefore the penalized non-linear least-squares equation

$$\psi = \frac{1}{2}\left(\boldsymbol{y} - \mathbf{B}\mathrm{e}^{-\mathbf{A}\boldsymbol{\mu}}\right)^T \mathbf{W}\left(\boldsymbol{y} - \mathbf{B}\mathrm{e}^{-\mathbf{A}\boldsymbol{\mu}}\right) + \beta\,\mathrm{R}(\boldsymbol{\mu}), \quad (3)$$

where R is a penalty function which returns a scalar and β is the penalty strength. The weighting matrix $\mathbf{W}$ in (3) is the inverse of the covariance matrix $\mathbf{K}$ in the forward model (2). The objective function (3) is equivalent (within an additive constant) to

$$\psi_2 = \theta + \beta \, \mathrm{R}(\boldsymbol{\mu}), \quad (4)$$

where

$$\theta \triangleq \frac{1}{2}[\mathrm{e}^{-\mathbf{A}\boldsymbol{\mu}}]^T \mathbf{B}^T \mathbf{W} \mathbf{B} \mathrm{e}^{-\mathbf{A}\boldsymbol{\mu}} - \boldsymbol{y}^T \mathbf{W} \mathbf{B} \mathrm{e}^{-\mathbf{A}\boldsymbol{\mu}}. \quad (5)$$

The PL reconstruction using this model (2) is formed by finding the volume, $\boldsymbol{\mu}$, that minimizes the objective (4). Note that (4) is non-convex.

We derive an algorithm to optimize (4) in a manner similar to that of [32], i.e., minimizing a separable quadratic surrogate of the objective function at each iteration. Each surrogate matches the objective function in value and first derivative at an operating point, and otherwise majorizes the objective function. Such an optimization approach is desirable since separability permits a high degree of parallelization (e.g., facilitating implementation on high-performance GPUs), while the surrogates framework can guarantee monotonicity. However, there is a classic trade-off between parallel algorithms, which require many fast iterations, and sequential algorithms, which require fewer slow iterations. We opt for a separable/parallel algorithm as opposed to a sequential algorithm to avoid line searches and to take advantage of available GPU hardware. See [36] for a steepest-descent algorithm with the same objective function. In [32], separable surrogate functions are found for the data fit term and the penalty term (in this work given by θ and R, respectively). We use the same formulation for the penalty term surrogate, but require a new formulation for the data fit term surrogate. A series of surrogates are calculated for (5): Q, Q_2, and Q_3. Q is a surrogate to θ which is separable in an intermediate term, Q_2 is a quadratic surrogate to Q, and Q_3 is a surrogate to Q_2 which is both separable in $\boldsymbol{\mu}$ and quadratic, and can thus be easily minimized. Each surrogate function has the same function value and first derivative as θ at the current iterate ($\boldsymbol{\mu}^{(n)}$). Therefore, minimizing the final surrogate at every iteration will monotonically decrease θ [31]. The derivation can be found in Appendix A (Supplementary Materials[2]), and the result (GPL-BC) is summarized in Algorithm 1.

Additional modifications to this underlying update are also shown in Algorithm 1. Specifically, the algorithm uses the ordered-subsets approach [32] to accelerate estimation. The variable m denotes the subset index and subscripts in parentheses indicate that the argument is modified for the corresponding subset (e.g. $\mathbf{A}_{(m)}\boldsymbol{\mu}$ is a forward projection of $\boldsymbol{\mu}$ using only the projection angles in the mth subset). While p indexes the outer loop of iterations using all of the data, the current iterate n is permitted to take on fractional values indicating progress through the inner loop of ordered-subsets updates. Algorithm 1 also includes a second column of calculations to optionally apply Nesterov acceleration [37], [38] to further improve the rate of convergence. Note that using ordered subsets or

---

[2]available in the supplementary files/multimedia tab

acceleration results in an algorithm that might not converge (acceleration is only guaranteed to preserve convergence when the objective function is convex). However, in practice the number of subsets can be chosen such that updates are well-behaved. Additionally, ordered subsets and acceleration can be used to get close to the solution, followed by several iterations without subsets or acceleration. Computationally, each iteration requires one forward projection, two back projections, and one application of $\mathbf{B}^T \mathbf{WB}$.

B. Additional Implementation Details

We apply the proposed algorithm using a model of focal-spot blur and scintillator blur, where the latter adds spatial correlation to the noise. Both of these blurs can be represented as factors of the $\mathbf{B}$ matrix:

$$\mathbf{B} \triangleq \mathbf{B}_d \mathbf{B}_s \mathbf{G} \quad (6)$$

where $\mathbf{B}_s$ is focal-spot blur, $\mathbf{B}_d$ is scintillator blur, and $\mathbf{G}$ scales the data by the bare-beam photon flux per pixel. As discussed in [29], the covariance matrix of the measurements can be modeled as

$$\mathbf{K} = [\mathbf{B}_d \, D\{\boldsymbol{y}\}\mathbf{B}_d^T + D\{\sigma_{ro}^2\}] \quad (7)$$

where σ_{ro} is the standard deviation of the readout noise and $D\{\cdot\}$ is a diagonal matrix with its argument on the diagonal. The weighting matrix $\mathbf{W}$ is equal to the inverse of $\mathbf{K}$, which is typically impractical to calculate explicitly. One approach [29] is to use an iterative linear solver to apply the inverse of $\mathbf{K}$ to the required vector argument. However, the vector argument is not constant, requiring that the iterative solution be performed every iteration, substantially increasing the runtime of the algorithm. However, note that within the iterative section of the algorithm $\mathbf{W}$ only appears in the term $\mathbf{B}^T \mathbf{WB}$. One can make the following approximation:

$$\mathbf{B}^T \mathbf{WB} = \mathbf{G}^T \mathbf{B}_s^T \mathbf{B}_d^T [\mathbf{B}_d \, D\{\boldsymbol{y}\}\mathbf{B}_d^T + D\{\sigma_{ro}^2\}]^{-1} \mathbf{B}_d \mathbf{B}_s \mathbf{G} \quad (8)$$

$$\approx \mathbf{G}^T \mathbf{B}_s^T \mathbf{B}_d^T [\mathbf{B}_d \, D\{\boldsymbol{y}\}\mathbf{B}_d^T]^{-1} \mathbf{B}_d \mathbf{B}_s \mathbf{G} \quad (9)$$

$$= \mathbf{G}^T \mathbf{B}_s^T \, D\{1/\boldsymbol{y}\}\mathbf{B}_s \mathbf{G}. \quad (10)$$

Equation 10 can be applied directly for each iteration, and is accurate when readout noise is small relative to the measurements, $\mathbf{B}_d$ is invertible, and all measurements are greater than 0.

Note that $\mathbf{B}^T\mathbf{WB}$ is only the weighting term, so removing $\mathbf{B}_d$ from this term is not equivalent to removing scintillator blur from the model. Scintillator blur is still included in other applications of $\mathbf{B}$ (see next paragraph). Additionally, (10) ensures η (see Algorithm 1) is always positive (a requirement of the optimum curvature derivation, see Appendix B, Supplementary Materials[3]) as long as $\mathbf{B}_s$ and $\mathbf{G}$ are non-negative, all diagonal elements of $\mathbf{G}$ are positive, and $\mathbf{B}_s$ has no rows or columns of all zeros.

The inverse covariance matrix is also included in the term $\mathbf{B}^T\mathbf{W}y$, which appears in the initialization section of the algorithm. In this work 200 iterations of a preconditioned conjugate gradient method [39], [40] were used to calculate this term. The preconditioning matrix was $\mathrm{D}\{y + \sigma_{ro}^2\}$.

C. System Characterization

To evaluate the proposed reconstruction method, scintillator and focal-spot blur properties of a prototype extremities qCBCT test bench [4] were first characterized. This characterization was then used to ensure an accurate simulation study (§II-D) and to generate accurate blur models for GPL-BC reconstructions of physical test-bench data (§II-E). The test bench uses an IMD RTM37 rotating anode X-ray source (with dual 0.3/0.6 focal spots) and a Teledyne DALSA Xi-neos3030HR CMOS X-ray detector (100 μm pixel pitch and CsI scintillator). The geometry emulates that of a prototype extremities qCBCT system, with a source-to-detector distance of 51 cm and a source-to-axis distance of 38 cm. X-ray focal-spot and detector blur were estimated from a pinhole image of the focal spot, edge spread function (ESF) measurements at the detector (where focal-spot blur is negligible), and ESF measurements at isocenter. The readout noise (σ_{ro}) was estimated using dark scans.

Images of a tungsten edge were used to calculate ESFs, which in turn were used to calculate modulation transfer functions (MTFs) as described in [29], [41]. MTFs were measured in two directions along the detector: parallel to the axes of rotation (axial) and perpendicular to the axis of rotation (trans-axial). This work assumes the detector scintillator MTF is radially symmetric and uses the model of [42] with an additional Gaussian component to capture observed low frequency characteristics:

$$MTF_d = g\mathrm{e}^{-f^2/\sigma^2} + (1-g)(1+Hf^2)^{-1} \quad (11)$$

where f is frequency and g is the relative strength of the Gaussian term (between 0 and 1). Combined with pixel sampling, the MTF model at the detector is

$$MTF_{da} = \mathrm{sinc}(fT)MTF_d \quad (12)$$

---

[3] available in the supplementary files/multimedia tab

where T is the pixel pitch. Because the pixels are square and the scintillator MTF is assumed to be radially symmetric, (12) models both the horizontal and vertical MTFs. We estimated the parameters g, σ, and H by fitting (12) to the MTFs measured at the detector.

Pinhole images of the X-ray focal spot were acquired using a 07–633 pinhole assembly (Fluke Electronics, Everett, WA) with a nominal diameter of 0.010 mm. A point spread function (PSF) that models the focal-spot blur experienced by an object at isocenter was found using this pinhole image. Because the pinhole was imaged at a high magnification (~34), multiple manipulations were required to obtain the final PSF. First, scale factors were found for each axes to match the shape of the pinhole image to that of the focal-spot PSF at isocenter. We chose the scaling parameters by fitting the axial and trans-axial slices of the pinhole derived MTF to the MTFs measured with the tungsten edge at isocenter. The axial and trans-axial scaling parameters are not necessarily the same due to different shift-variant properties in these two directions, and the possibility that the pinhole was slightly misaligned. The pinhole image was resampled using these scaling parameters to produce a super-sampled PSF of the focal-spot blur at isocenter. In order to account for the aperture of each pixel, the super-sampled PSF was convolved with a 100 μm × 100 μm rect function corresponding to the pixel pitch and then binned and normalized to produce a PSF with 100 μm pixels (i.e., in native measurement dimensions).

D. Simulation Study

Data were generated using the digital phantom in Fig. 1 and a simulated system model based on the test bench geometry and characterization. Specifically, the high-resolution phantom was created with 17.5 μm × 17.5 μm × 70 μm voxels (with the long axis of the voxel parallel to the axis of rotation) and high contrast line pairs with an attenuation of 0.060 mm^{-1} (bone) and a background attenuation of 0.019 mm^{-1} (fat). To model nonlinear partial volume effects, this phantom was forward projected onto a 87.5 mm detector of subpixels with a small pixel pitch (25 μm × 100 μm) at 720 equally spaced angles using a separable footprints model [43] for the projector. The forward model for data generation used finite integration over the extended focal spot and detector elements:

$$y = \mathbf{S}\widetilde{\mathbf{B}}_\mathrm{d}\widetilde{\mathbf{G}} \sum_k^{n_k} \omega_k e^{-\mathbf{A}_k \mu} \quad (13)$$

where $\mathbf{A}_k$ is a projection matrix corresponding to an individual sourcelet with relative intensity ω_k, $\widetilde{\mathbf{B}}_\mathrm{d}$ is a scintillator blur (11) matrix which operators on subpixels, $\widetilde{\mathbf{G}}$ scales the subpixels by the photon flux, and $\mathbf{S}$ bins the subpixels to 100 μm × 100 μm pixels. To obtain a final photon flux of 10^3 photons pixel^{-1}, $\widetilde{\mathbf{G}}$ scaled each subpixel by 250 photons pixel^{-1}. The scintillator blur matrix was applied functionally using Fourier operations and nearest neighbor substitution at the boundaries. Focal-spot blur was modeled by forward projecting with 354 sourcelets derived from the super-sampled PSF from §II-C (summed to one dimension). The modeled anode angle was 17.5°. Noisy data were generated from a Poisson distribution with the Poisson parameter equal to the pre-scintillator-blur data (e.g., the vector before application of $\widetilde{\mathbf{B}}_\mathrm{d}$), and these noisy data were blurred by $\widetilde{\mathbf{B}}_\mathrm{d}$. Finally, we added

Gaussian readout noise with a standard deviation of 7.109 photons (based on bench data dark scan values) to obtain the final measurements.

In all simulation studies the reconstruction volume was 70 mm $\times$ 35 mm with 0.07 mm cubic voxels (i.e., approximately equal to the demagnified pixel size). Data were reconstructed with the presented GPL-BC algorithm incorporating the blur models derived in §II-C. Specifically, $\mathbf{B}$ in (6) was applied, where $\mathbf{B}_s$ and $\mathbf{B}_d$ convolve their inputs with the focal-spot PSF (summed to one dimension) and the scintillator blur (11), respectively, and $\mathbf{G}$ scales each value by 10^3 photons pixel^{-1}. With the low photon flux of the simulation study, the measurement data is not substantially higher than readout noise, and (10) is not a valid approximation. Therefore, 20 iterations of the preconditioned conjugate gradient method were used to apply $\mathbf{W}$ every iteration. For comparison, the same optimization strategy was used with two different forward models. The first, GPL-B, assumed the noise was uncorrelated (i.e., $\mathbf{K} = D\{y + \sigma_{ro}^2\}$). The second, GPL-I, also assumed the noise was uncorrelated, and additionally assumed there was no blur (i.e., $\mathbf{B} = \mathbf{G}$). Finally, the data were also reconstructed using Fourier domain deblurring (using the same blur models as GPL-B and GPL-BC) followed by FDK (dFDK) with multiple cutoff frequencies. All model-based reconstructions used the separable footprints projector [43].

Reconstructions were assessed with three metrics: bias, noise, and maximum Jaccard index (mJac) [44]. Bias and noise were chosen as traditional image quality metrics, while mJac was picked as a metric specific to trabecular bone analysis. These metrics were calculated for the set of line pairs in the middle of Figure 1. The terms are defined based on the truth image t (binned to match voxel size), reconstructions of noiseless data $\hat{\boldsymbol{\mu}}_{nl}(\beta, \delta)$, reconstructions of noisy data $\hat{\boldsymbol{\mu}}(\beta, \delta)$, and the number of voxels in the ROI (N_{roi})

$$\text{bias}(\beta, \delta) = \|\hat{\boldsymbol{\mu}}_{nl}(\beta, \delta) - t\|/N_{roi} \quad (14)$$

$$\text{noise}(\beta, \delta) = \|\hat{\boldsymbol{\mu}}(\beta, \delta) - \hat{\boldsymbol{\mu}}_{nl}(\beta, \delta)\|/N_{roi}. \quad (15)$$

These metrics were calculated in an ROI encompassing the central line pairs. To calculate mJac, a truth segmentation t_b was calculated by thresholding the truth image t at 0.040 mm^{-1} (the average attenuation value of fat and bone). The reconstruction $\hat{\boldsymbol{\mu}}$ was thresholded by a value t for 101 values of t between the attenuation values of fat and bone, inclusive. The mJac value for a given reconstruction is the maximum Jaccard index between the truth segmentation and the segmented $\hat{\boldsymbol{\mu}}$ over all t:

$$\text{mJac}(\beta, \delta) = \max_t \left[\text{Jaccard}\left(\hat{\boldsymbol{\mu}}(\beta, \delta) > t, t_b\right) \right]. \quad (16)$$

The Jaccard index ranges from 0 to 1, with 1 indicating perfect correspondence with the truth segmentation.

1) Parameter Sweep—This work used a Huber penalty for the regularizer (R) [45]. The Huber penalty has an additional parameter, δ, which is the value below which pixel differences will be penalized quadratically. We conducted a parameter sweep over β and δ in order to pick an appropriate value for δ. Phantom data were reconstructed using GPL-BC and GPL-I. Additionally, two photon fluxes were used: 10^3 photons pixel^{-1} (low photon flux) to match the simulation study, and 4×10^4 photons pixel^{-1} (high photon flux) to approximate the bench study. The high photon flux data utilized the covariance matrix approximation in (10). Both algorithms used 501 iterations, 10 subsets, and momentum-based acceleration. The mJac metric was calculated for each (β, δ) pair.

2) Algorithm Comparison—dFDK, GPL-I, GPL-B, and GPL-BC were compared by analyzing the bias/noise tradeoff and mJac over a range of regularization strengths. A large number of iterations (20 000) were used to ensure nearly converged estimates. We utilized a scheduling approach for acceleration and the number of subsets, with 50 iterations of acceleration and 10 subsets, followed by 50 iterations of acceleration and 5 subsets, 10 000 iterations of acceleration and no subsets, and finally 9000 iterations of no acceleration and no subsets. We used a Huber penalty with $\delta = 10^{-2}$ mm^{-1}. A bias/noise plot and a plot of mJac as a function of β were analyzed for the center set of line pairs in Figure 1 and each of the four reconstruction methods. For direct visual comparison we present reconstructions of the line pairs, along with the corresponding optimum segmentations.

E. Bench Data

To investigate the performance of the proposed algorithm on physical data, a human iliac-crest bone-biopsy core was scanned on the test bench described in §II-C. The bone sample comprised both trabecular and cortical bone. **B** was modeled as described previously (6), with $\mathbf{B}_s$ and $\mathbf{B}_d$ representing applications of the models developed in §II-C. Blur matrices were applied functionally as in the simulation study. $\mathbf{B}_d$ was applied using Fourier methods and $\mathbf{B}_s$ was applied using convolution. The covariance approximation (10) was used. **G** was a matrix which scaled the values of each pixel by the estimated bare-beam photon flux and each frame by a normalization factor.[4] The projection operator **A** used the separable footprints algorithm as in the simulation study. The GPL methods used the same readout noise value as the simulation study.

Reconstructions were initialized with FDK and ran for 650 iterations with 10 subsets to obtain well-converged estimates. The trabecular bone was also reconstructed with GPL-I and GPL-B using the same number of iterations and subsets. Momentum-based acceleration was applied in all cases. A Huber regularization penalty was used with a range of penalty strengths and δ equal to 10^{-3} mm^{-1} [45]. We also computed an FDK reconstruction (frequency cutoff at Nyquist and no additional apodization) for comparison. In all cases the reconstruction volume was 60 mm $\times$ 60 mm $\times$ 30 mm with 0.075 mm voxels (i.e., voxel size was approximately equal to the demagnified pixel size). The projection area was 120 mm $\times$ 25 mm with 0.1 mm pixel pitch and 720 frames.

---

[4]Details are given in Appendix C in the supplementary material, available in the supplementary files/multimedia tab.

Reconstructions of qCBCT data were compared with high resolution μCT data using mJac (16), Trabecular Thickness (Tb.Th.), Trabecular Spacing (Tb.Sp.), and Bone Volume to Total Volume fraction (BV/TV) [33]–[35]. Bench data were acquired at 90 kV and 90.7 mA s. The μCT data were acquired on a SkyScan 1172 CT scanner (Bruker microCT, Kontich, Belgium) at 65 kV. To find the "true" trabecular bone segmentation with the same voxel size as the reconstructions, the μCT image of the trabecular bone was first binned from 0.0076 mm voxel^{-1} to 0.0380 mm voxel^{-1} and then registered with an FDK reconstruction of the qCBCT bench data. The registration algorithm also reduced the voxel size of the μCT image to match that of the FDK reconstruction (and therefore the model-based reconstructions). The resulting image is referred to as μCTmv for Matched Voxel size. The Elastix software package [46] registered the images using the binned μCT reconstruction as the moving image, a similarity transformation, and the Mutual Information Metric. A mask was used to limit the evaluation of the registration metric to a sub-volume containing only trabecular bone. The μCTmv image was thresholded to generate the "truth segmentation." The threshold value was chosen using a visual histogram inspection. The FDK, GPL-I, GPL-B, and GPL-BC reconstructions were thresholded at 101 equally spaced attenuation values between 0 mm^{-1} and 0.07 mm^{-1}, inclusive, to calculate mJac. The mJac metric was only computed within the trabecular region (using the same mask as the registration). This metric was plotted for each MBIR reconstruction method as a function of regularization strength. The most accurate segmented reconstruction from each MBIR method was selected as the one with the highest mJac over all regularization strengths, and the most accurate reconstruction was selected as the corresponding pre-thresholded image. The optimal FDK segmentation was defined as the one with the highest mJac over all threshold values. A Tb.Th. map was calculated from the optimal segmented reconstruction for each reconstruction method and the μCTmv image. Tb.Th. and Tb.Sp. were calculated with BoneJ [47], a plug-in for ImageJ [48]. Average Tb.Th., Tb.Sp, and BV/TV were computed over the area defined by the registration/mJac mask. The Tb.Th. and BV/TV of the original μCT image (before binning and registration) were also calculated using the same mask (transformed to the μCT coordinates). (Tb.Sp. was not calculated for this image due to computation constraints.) Slices of the μCT scan and μCT Tb.Th. map were transformed using the registration parameters calculated previously, facilitating visual comparison to the other methods. Optimal reconstructions, optimal segmentations, and Tb.Th. maps for FDK, GPL-I, GPL-B, and GPL-BC were compared with corresponding μCTmv and original μCT images.

III. Results

A. System Characterization

The system characterization results are shown in Fig. 2. The measured MTFs are plotted in Fig. 2A and show that, for the prototype test bench, detector blur is a larger effect than focal-spot blur. Because detector blur (scintillator blur and pixel aperture blur) is the same at the detector and at isocenter, the difference between the isocenter MTF and the detector MTF is due to focal spot blurring. This difference is relatively small, indicating that this system is dominated by detector blur. The axial and trans-axial detector MTFs are almost equivalent,

supporting the radially symmetric assumption used in the model. The MTF models (Fig. 2B) strongly match the measured data.

The focal-spot pinhole image was scaled and resampled to match the magnitude of the blur experienced by an object at isocenter (Fig. 2). The focal spot has a primary trapezoidal component with a higher intensity on two of the edges, similar to those observed on the rectangular focal spot studied previously [29]. This focal spot has an additional, lower intensity, trapezoidal component with a different orientation, creating a cross pattern. Because of this complicated structure, we decided to derive a PSF directly from the pinhole image instead of using a mathematical model. The scale bar illustrates that the focal spot blur is relatively small (about the size of a detector pixel) for an object at isocenter.

B. Simulation Study

1) Parameter Sweep—Fig. 3 shows the maximum mJac over β as a function of δ for two noise realizations. These results indicate that mJac is relatively insensitive to δ (compare the ranges in the plots in Fig. 3 to those in Fig. 4). This is potentially due to the fact that mJac is insensitive to edge smoothness. The measurements are relatively noisy at this scale, especially with low gain and low δ. For GPL-BC the optimal δ is higher than any contrast in the phantom, indicating a "near" quadratic penalty is ideal. The simulation data were reconstructed with $\delta = 10^{-2}$ mm^{-1} (where mJac values are high and stable) and the bench data with $\delta = 10^{-3}$ mm^{-1} (which potentially gives a slight advantage to GPL-I).

Figure 4 shows the bias/noise trade-off (A) and maximum Jaccard index (B) for the center set of line pairs. Results are similar but less dramatic for the other two sets of line pairs (not shown). At lower regularization strengths, reconstructions of noiseless data are more accurate (lower bias), but reconstructions of noisy data result in noisy reconstructions. On the other hand, for higher regularization strengths, noise is suppressed at the cost of increased smoothing/blurring of the image, imparting bias. Methods with blur modeling (GPL-BC and GPL-B) were able to achieve a lower bias than the method without blur modeling (GPL-I). GPL-BC and GPL-B have a similar bias/noise trade-off, with GPL-BC showing a slight advantage. Because it does not include a blur model, GPL-I encounters a bias limit at about 0.013 mm^{-1}. dFDK can achieve lower bias reconstructions than GPL-I, but suffers from increased noise as compared to GPL-B and GPL-BC. However, there is a small range (near the best dFDK mJac performance) where dFDK performs comparably to GPL-B and GPL-BC.

Figure 4B shows similar trends. For each method the "best" reconstruction is defined as the one with the maximum mJac. This maximum mJac value is used to compare the different methods. GPL-BC results in the best reconstruction, followed by GPL-B, dFDK, and GPL-I. The advantage of GPL-BC over GPL-B is more apparent in the mJac plot than the bias/noise plot.

Figure 5 shows reconstructions of the center line pairs. The bottom half of each image shows the optimal segmentation (i.e., the one resulting in the best mJac). GPL-I results in the worst performance with low contrast line pairs. The line pairs in the dFDK reconstruction are more distinct but both the line pairs and the background exhibit increased noise. Finally, the GPL-

B and GPL-BC reconstructions have less noise than the dFDK reconstruction without sacrificing line pair visualization. The difference between the GPL-BC and GPL-B reconstructions is subtle, but can be appreciated in the thresholded image, where the GPL-BC method results in thicker and more uniform line pairs. The noise difference between GPL-BC/GPL-B and dFDK is particularly evident in the background of the segmented image, where the dFDK reconstruction contains noisy values above the segmentation threshold, resulting in a "splotchy" segmented background image. Qualitatively, the visually "best" reconstructions correspond to those with the best mJac (indicated by a red outline), confirming the suitability of this metric.

C. Bench Data

This section presents the results of the prototype test-bench study with human trabecular bone. The mJac for each reconstruction is shown as a function of regularization strength in Fig. 6. The GPL-BC method is able to achieve the highest maximum mJac, followed by GPL-B, GPL-I, and FDK (indicated by the black line). The optimal segmentation thresholds for the most accurate GPL-I, GPL-B, and GPL-BC reconstructions (i.e., those with the maximum mJac over regularization strength, corresponding to the maxima in Fig. 6) are 0.0322 mm^{-1}, 0.0385 mm^{-1}, and 0.0378 mm^{-1}, respectively.

The most accurate reconstructions are shown in Fig. 7 and Fig. 8, along with the corresponding segmented trabecular bone images (using the optimal thresholds) and Tb.Th. maps. The FDK reconstruction, the registered μCT reconstruction with Matched Voxel size (μCTmv), and the registered μCT reconstruction slices with the original μCT voxel size (μCT) are also included. While the μCT reconstruction is the best approximation of the true image volume, the μCTmv image is a better approximation of the best achievable reconstruction at the chosen voxel size.

The GPL-BC reconstruction has improved resolution as compared to the GPL-B, GPL-I, and FDK reconstructions, with sharper trabecular bone boundaries. Consequently, GPL-BC results in a more accurate trabecular segmentation. This is particularly evident when comparing to FDK and GPL-I, where the segmentation images contain less detailed trabeculae. This effect is well illustrated in the Tb.Th. maps. The FDK and GPL-I maps show fewer, thicker trabeculae, while the GPL-BC map is similar to the μCTmv and μCT maps with thinner and more numerous trabeculae. The GPL-B map is more similar to the GPL-BC map, but still contains thicker trabeculae. The mean Tb.Th. calculations (Table II) confirm this observation, with GPL-BC resulting in a Tb.Th. value closer to those of μCTmv and μCT than do FDK, GPL-I, and GPL-B. In contrast, GPL-BC shows no advantage with respect to Tb.Sp. and BV/TV. BV/TV values are similar for all methods, suggesting the loss of fine trabecular structures and the increase in apparent trabecular thickness tend to cancel each other out in terms of BV/TV. The same mechanism is a potential cause for the better accuracy of the FDK and GPL-I mean Tb.Sp. values: the spacing lost to thicker trabeculae is recovered by the loss of fine trabeculae. In contrast, GPL-BC does a better job in general at recovering small trabeculae, but still reconstructs trabeculae as thicker than they should be, reducing the mean Tb.Sp. Optimizing reconstructions based on one of these metrics instead of mJac may improve metric accuracy, or show that GPL-BC is ill-suited to that metric.

IV. Discussion

We have presented a generalized reconstruction algorithm (GPL-BC) capable of utilizing a variety of high fidelity CBCT system models, which may include focal-spot blur, scintillator blur, and correlated noise. We evaluated this method in a scintillator blur dominated scenario in simulation and on a prototype CBCT test bench. These studies show that high fidelity modeling with GPL-BC can improve resolution and produce more accurate reconstructions as compared to more traditional models and FDK approaches. The improved accuracy of the trabecular bone segmentation and Tb.Th. measurement suggest that GPL-BC can increase the accuracy of quantitative metrics used to study trabecular bone health [6], [49], [50]. Additionally, the improved bias/noise trade-off suggests that GPL-BC produces more accurate attenuation values than dFDK and GPL-I, which is critical for quantitative CT [51] (however, note that bias includes both attenuation value error and blurring).

While this work utilizes a relatively simple mathematical formulation, we note that GPL-BC is capable of incorporating a wide variety of complicated models. For example, one can extend the model here to incorporate a shift-variant blur and depth-dependence (focal-spot blur) [24], [52] with proper definition of $\mathbf{B}$ or $\mathbf{A}$. The model may also incorporate detector lag (a temporal blur function) with a similar redefinition of $\mathbf{B}$ and blur due to gantry motion with modifications to both $\mathbf{A}$ and $\mathbf{B}$. The only constraints are that $\mathbf{A}$, $\mathbf{B}$, and $\mathbf{W}$ are matrices and η is positive. Such modifications are the subject of ongoing and future work.

As algorithms enable increased resolution, proper choice of voxel size will be critical [53]. If one were not attempting resolution recovery, the ideal voxel size would be about the size of the demagnified system blur (0.33 mm for this system). (The large system blur relative to pixel pitch results in most CBCT systems binning projection data to increase effective pixel pitch.) In this work voxel size was approximately equal to the demagnified pixel pitch (i.e., much smaller than the limit imposed by system blur). Angular sampling also effects voxel size. CT data is almost always angularly undersampled. To limit the effect of undersampling we acquire data in half angle increments (double the sampling of traditional CBCT). In summary, we believe the choices of voxel size and angular sampling in this work are appropriate for the system blur studied, and allow a fair comparison of the different MBIR system models.

While not a focus of this study, we note that incorporating blur into the model decreases the convergence rate. In order to compare nearly converged solutions, many iterations were used. (This is particularly important for regularization sweeps, as different regularization strengths may require different numbers of iterations.) However, we believe that tuning the subset/acceleration schedule can improve the convergence rate in practice. With the current (only partially optimized) implementation, the bench data reconstructions took approximately 10–15 min per iteration. (Note the reconstruction volume was much larger than the ROI shown.) When the ROI is small, as in this work, a multi-resolution reconstruction method may be employed to decrease iteration time [54].

The main limitation of the objective function presented is the application of the inverse covariance matrix, which may be computationally expensive if noise correlations are

modeled. In the bench data study, we make assumptions to avoid computing this inversion every iteration, but such assumptions will not always be valid (as in the simulation study). In such cases, one may need to make additional approximations to reduce computation time. Additionally, patient motion may be a resolution limiting factor on high-resolution systems. However, if patient motion is properly estimated, it may be incorporated into the system matrix to reduce this image degradation without altering the presented algorithm [55].

The success of MBIR methods illustrates the importance of high-fidelity modeling in CT reconstruction. Accurate modeling of CBCT systems, enabled by the proposed method, improves image quality and permits high-resolution tasks such as microcalcification detection and analysis of trabecular bone morphology. In addition to improving the capabilities of current CBCT systems, this method has the potential to alter the trade-offs between hardware/geometry choices and image quality, potentially effecting future CBCT system designs, including those that aren't necessarily aiming for high resolution. For example, proper focal-spot modeling may better leverage high-magnification or permit replacing rotating-anode X-ray sources with more economical fixed-anode sources while preserving resolution. Future studies will characterize the improvements possible with the proposed GPL-BC approach and their possible impact on CBCT system design, in addition to incorporating the different blur models described above and considering systems with different balances of correlating and non-correlating blur.

Supplementary Material

Refer to Web version on PubMed Central for supplementary material.

Acknowledgments

References

1. Lai CJ, Shaw CC, Chen L, Altunbas MC, Liu X, Han T, Wang T, Yang WT, Whitman GJ, Tu SJ. Visibility of microcalcification in cone beam breast CT: Effects of X-ray tube voltage and radiation dose. Medical Physics. 2007; 34(7):2995–3004. [PubMed: 17822008]

2. Kwan ALC, Boone JM, Yang K, Huang SY. Evaluation of the spatial resolution characteristics of a cone-beam breast CT scanner. Medical Physics. 2007; 34(1):275–281. [PubMed: 17278513]

3. Carrino JA, Al Muhit A, Zbijewski W, Thawait GK, Stayman JW, Packard N, Senn R, Yang D, Foos DH, Yorkston J, Siewerdsen JH. Dedicated cone-beam CT system for extremity imaging. Radiology. 2014; 270(3):816–24. [PubMed: 24475803]

4. Marinetto, E., Brehler, M., Sisniega, A., Cao, Q., Stayman, JW., Yorkston, J., Siewerdsen, JH., Zbijewski, W. Quantification of bone microarchitecture in ultrahigh resolution extremities conebeam CT with a CMOS detector and compensation of patient motion. Computer Assisted Radiology 30th International Congress and Exhibition; Heidelberg, Germany. Jun. 2016;

5. Gong X, Vedula AA, Glick SJ. Microcalcification detection using cone-beam CT mammography with a flat-panel imager. Physics in Medicine and Biology. 2004; 49(11):2183–2195. [PubMed: 15248571]

6. Griffith JF, Genant HK. New imaging modalities in bone. Current Rheumatology Reports. 2011; 13(3):241–250. [PubMed: 21369797]

7. Baba R, Ueda K, Okabe M. Using a flat-panel detector in high resolution cone beam CT for dental imaging. Dentomaxillofacial Radiology. Sep; 2004 33(5):285–290. [PubMed: 15585803]

8. Bamba J, Araki K, Endo A, Okano T. Image quality assessment of three cone beam CT machines using the SEDENTEXCT CT phantom. Dentomaxillofacial Radiology. Aug.2013 42(8):20120445. [PubMed: 23956235]

9. Thibault JB, Sauer KD, Bouman CA, Hsieh J. A three-dimensional statistical approach to improved image quality for multislice helical CT. Medical Physics. 2007; 34(11):4526. [PubMed: 18072519]

10. Feldkamp LA, Davis LC, Kress JW. Practical cone-beam algorithm. J Opt Soc Am A. Jun; 1984 1(6):612–619.

11. Wang AS, Stayman JW, Otake Y, Kleinszig G, Vogt S, Gallia GL, Khanna AJ, Siewerdsen JH. Soft-tissue imaging with C-arm cone-beam CT using statistical reconstruction. Physics in Medicine and Biology. Feb; 2014 59(4):1005–1026. [PubMed: 24504126]

12. Dang H, Stayman JW, Sisniega A, Xu J, Zbijewski W, Wang X, Foos DH, Aygun N, Koliatsos V, Siewerdsen JH. Statistical Reconstruction for Cone-Beam CT with a Post-Artifact-Correction Noise Model: Application to High-Quality Head Imaging. Physics in Medicine and Biology. 2015; 60(16):6153–6175. [PubMed: 26225912]

13. Sun T, Sun N, Wang J, Tan S. Iterative CBCT reconstruction using Hessian penalty. Physics in Medicine and Biology. 2015; 60(5):1965–1987. [PubMed: 25674998]

14. Hofmann, C., Knaup, M., Kachelriess, M. Do We Need to Model the Ray Profile in Iterative Clinical CT Image Reconstruction?. Radiological Society of North America Annual Meeting; Chicago. 2013. p. 403

15. Hofmann C, Knaup M, Kachelrieβ M. Effects of ray profile modeling on resolution recovery in clinical CT. Medical Physics. Feb.2014 41(2) n/a–n/a.

16. Tsui BMW, Hu HB, Gilland DR, Gullberg GT. Implementation of Simultaneous Attenuation and Detector Response Correction in Spect. IEEE Transactions on Nuclear Science. 1987; 35(1):778–783.

17. Qi J, Leahy RM, Hsu C, Farquhar TH, Cherry SR. Fully 3D Bayesian image reconstruction for the ECAT EXACT HR+ IEEE Transactions on Nuclear Science. Jun; 1998 45(3):1096–1103.

18. Qi J, Leahy RM, Cherry SR, Chatziioannou A, Farquhar TH. High-resolution 3D Bayesian image reconstruction using the microPET small-animal scanner. Physics in Medicine and Biology. 1998; 43(4):1001. [PubMed: 9572523]

19. Formiconi AR, Pupi A, Passeri A. Compensation of spatial system response in SPECT with conjugate gradient reconstruction technique. Physics in Medicine and Biology. 1989; 34(1):69. [PubMed: 2784572]

20. Chun SY, Fessler Ja, Dewaraja YK. Correction for collimator-detector response in SPECT using point spread function template. IEEE Transactions on Medical Imaging. 2013; 32(2):295–305. [PubMed: 23086521]

21. Alessio AM, Kinahan PE, Lewellen TK. Modeling and incorporation of system response functions in 3-D whole body PET. IEEE Transactions on Medical Imaging. Jul; 2006 25(7):828–837. [PubMed: 16827484]

22. Alessio A, Sauer K, Bouman CA. MAP Reconstruction From Spatially Correlated PET Data. IEEE Transactions on Nuclear Science. 2003; 50(5):1445–1451.

23. La Rivière PJ, Bian J, Vargas PA. Penalized-likelihood sinogram restoration for computed tomography. IEEE Transactions on Medical Imaging. Aug; 2006 25(8):1022–36. [PubMed: 16894995]

24. La Riviere PJ, Vargas P. Correction for resolution nonuniformities caused by anode angulation in computed tomography. IEEE Transactions on Medical Imaging. 2008; 27(9):1333–1341. [PubMed: 18779068]

25. Zhang H, Ouyang L, Ma J, Huang J, Chen W, Wang J. Noise correlation in CBCT projection data and its application for noise reduction in low-dose CBCT. Medical Physics. Mar.2014 41(3): 031906. [PubMed: 24593724]

26. Yu DF, Fessler JA, Ficaro EP. Maximum-likelihood transmission image reconstruction for overlapping transmission beams. IEEE Transactions on Medical Imaging. Nov; 2000 19(11):1094–105. [PubMed: 11204847]

27. Feng B, Fessler JA, King MA. Incorporation of system resolution compensation (RC) in the ordered-subset transmission (OSTR) algorithm for transmission imaging in SPECT. IEEE Transactions on Medical Imaging. Jul; 2006 25(7):941–9. [PubMed: 16827494]

28. Zheng J, Fessler JA, Chan H-P. Detector Blur and Correlated Noise Modeling for Digital Breast Tomosynthesis Reconstruction. IEEE Transactions on Medical Imaging. 2017

29. Tilley S II, Siewerdsen JH, Stayman JW. Model-based iterative reconstruction for flat-panel cone-beam CT with focal spot blur, detector blur, and correlated noise. Physics in Medicine and Biology. 2016; 61(1):296. [PubMed: 26649783]

30. Tilley S II, Siewerdsen JH, Zbijewski W, Stayman JW. Nonlinear statistical reconstruction for flat-panel cone-beam CT with blur and correlated noise models. SPIE 9783 Medical Imaging 2016: Physics of Medical Imaging. 2016; 9783:97 830R–6.

31. Erdo an H, Fessler JA. Monotonic algorithms for transmission tomography. IEEE Transactions on Medical Imaging. Sep; 1999 18(9):801–14. [PubMed: 10571385]

32. Erdo an H, Fessler J. Ordered subsets algorithms for transmission tomography. Physics in Medicine and Biology. 1999; 2835

33. Ding M, Hvid I. Quantification of age-related changes in the structure model type and trabecular thickness of human tibial cancellous bone. Bone. Mar; 2000 26(3):291–295. [PubMed: 10710004]

34. Hildebrand T, Rüegsegger P. A new method for the model-independent assessment of thickness in three-dimensional images. Journal of Microscopy. Jan; 1997 185(1):67–75.

35. Bouxsein ML, Boyd SK, Christiansen BA, Guldberg RE, Jepsen KJ, Müller R. Guidelines for assessment of bone microstructure in rodents using micro-computed tomography. Journal of Bone and Mineral Research. 2010; 25(7):1468–1486. [PubMed: 20533309]

36. Tilley, S., II, Siewerdsen, JH., Stayman, JW. SPIE Medical Imaging. San Diego, CA: 2016. Nonlinear Statistical Reconstruction for Flat-Panel Cone-Beam CT with Blur and Correlated Noise Models.

37. Nesterov Y. Smooth minimization of non-smooth functions. Mathematical Programming Journal, Series A. 2005; 103:127–152.

38. Kim D, Ramani S, Fessler JA. Combining Ordered Subsets and Momentum for Accelerated X-Ray CT Image Reconstruction. IEEE Transactions on Medical Imaging. 2015; 34(1):167–178. [PubMed: 25163058]

39. Nocedal, J., Wright, SJ. Numerical Optimization. 2. New York, NY, USA: Springer; 2006. ser. Springer Series in Operation Research and Financial Engineering

40. Hestenes MR, Stiefel E. Methods of conjugate gradients for solving linear systems. Journal of Research of the National Bureau of Standards. 1952; 49(6):409–436.

41. Samei E, Flynn MJ, Reimann DA. A method for measuring the presampled MTF of digital radiographic systems using an edge test device. Medical Physics. 1998; 25(1):102. [PubMed: 9472832]

42. Siewerdsen JH, Antonuk LE, El-Mohri Y, Yorkston J, Huang W, Cunningham IA. Signal, noise power spectrum, and detective quantum efficiency of indirect-detection flat-panel imagers for diagnostic radiology. Medical Physics. May; 1998 25(5):614–628. [PubMed: 9608470]

43. Long Y, Fessler JA, Balter JM. 3D forward and back-projection for X-ray CT using separable footprints. IEEE Transactions on Medical Imaging. Nov; 2010 29(11):1839–50. [PubMed: 20529732]

44. Jaccard P. The Distribution of the Flora in the Alpine Zone.1. New Phytologist. Feb; 1912 11(2): 37–50.

45. Huber, PJ. Robust Statistics. New York: Wiley; 1981.

46. Klein S, Staring M, Murphy K, Viergever MA, Pluim JPW. Elastix: A Toolbox for Intensity-Based Medical Image Registration. IEEE Transactions on Medical Imaging. Jan; 2010 29(1):196–205. [PubMed: 19923044]

47. Doube M, Kłosowski MM, Arganda-Carreras I, Cordelieres FP, Dougherty RP, Jackson JS, Schmid B, Hutchinson JR, Shefelbine SJ. BoneJ: Free and extensible bone image analysis in ImageJ. Bone. Dec; 2010 47(6):1076–1079. [PubMed: 20817052]

48. Schneider CA, Rasband WS, Eliceiri KW. NIH Image to ImageJ: 25 years of image analysis. Nature Methods. Jul; 2012 9(7):671–675. [PubMed: 22930834]

49. Mohan G, Perilli E, Parkinson IH, Humphries JM, Fazzalari NL, Kuliwaba JS. Pre-emptive, early, and delayed alendronate treatment in a rat model of knee osteoarthritis: Effect on subchondral trabecular bone microarchitecture and cartilage degradation of the tibia, bone/cartilage turnover, and joint discomfort. Osteoarthritis and Cartilage. 2013; 21(10):1595–1604. [PubMed: 23827368]

50. Issever AS, Link TM, Kentenich M, Rogalla P, Burghardt AJ, Kazakia GJ, Majumdar S, Diederichs G. Assessment of trabecular bone structure using MDCT: Comparison of 64- and 320-slice CT using HR-pQCT as the reference standard. European Radiology. Aug; 2009 20(2):458–468. [PubMed: 19711081]

51. Cann CE. Quantitative CT for determination of bone mineral density: A review. Radiology. Feb; 1988 166(2):509–522. [PubMed: 3275985]

52. Tilley S II, Zbijewski W, Siewerdsen JH, Stayman JW. Modeling shift-variant X-ray focal spot blur for high-resolution flat-panel cone-beam CT. Proc 4th Intl Mtg on Image Formation in X-Ray CT. 2016

53. Sidky EY, Duchin Y, Pan X, Ullberg C. A constrained, total-variation minimization algorithm for low-intensity x-ray CT. Medical Physics. Jul; 2011 38(S1):S117–S125. [PubMed: 21978112]

54. Cao Q, Zbijewski W, Sisniega A, Yorkston J, Siewerdsen JH, Stayman JW. Multiresolution iterative reconstruction in high-resolution extremity cone-beam CT. Physics in Medicine and Biology. 2016; 61(20):7263. [PubMed: 27694701]

55. Sisniega A, Stayman JW, Yorkston J, Siewerdsen JH, Zbi-jewski W. Motion compensation in extremity cone-beam CT using a penalized image sharpness criterion. Physics in Medicine and Biology (accepted). 2017

56. De Pierro AR. On the relation between the ISRA and the EM algorithm for positron emission tomography. IEEE Transactions on Medical Imaging. 1993; 12(2):328–333. [PubMed: 18218422]

57. Jacobson MW, Fessler JA. An Expanded Theoretical Treatment of Iteration-Dependent Majorize-Minimize Algorithms. IEEE Transactions on Image Processing. Oct; 2007 16(10):2411–2422. [PubMed: 17926925]

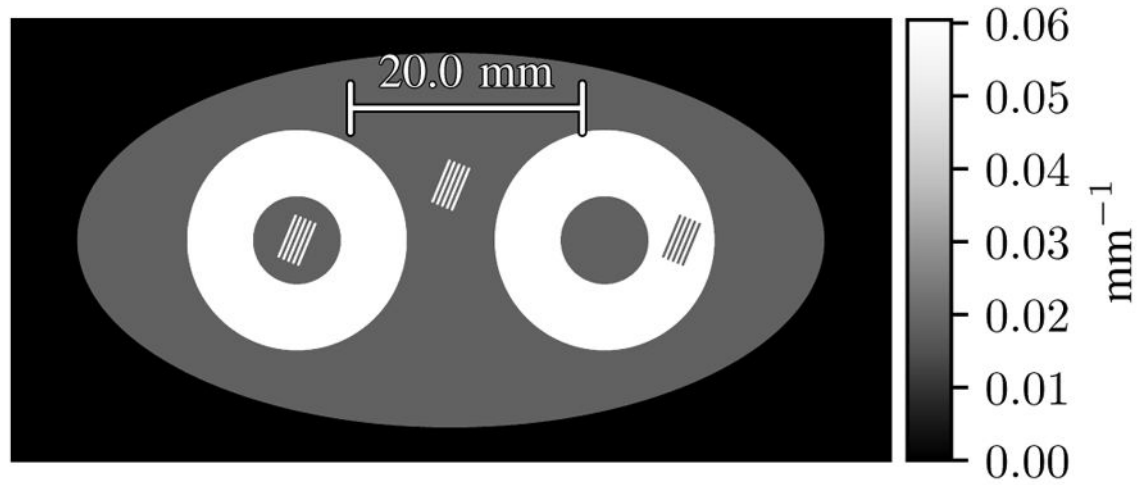58. Prince, JL., Links, J. Medical Imaging Signals and Systems. 1. Upper Saddle River, NJ: Prentice Hall; Apr. 2005

Fig. 1.
Digital phantom with line pairs and bone inserts. The background attenuation value in the oval is 0.019 mm^{-1} and the bone attenuation is 0.060 mm^{-1}. The line pair attenuation values are either 0.060 mm^{-1} (left and center) or 0.019 mm^{-1} (right). The line pair frequency is 2.38 mm^{-1}.
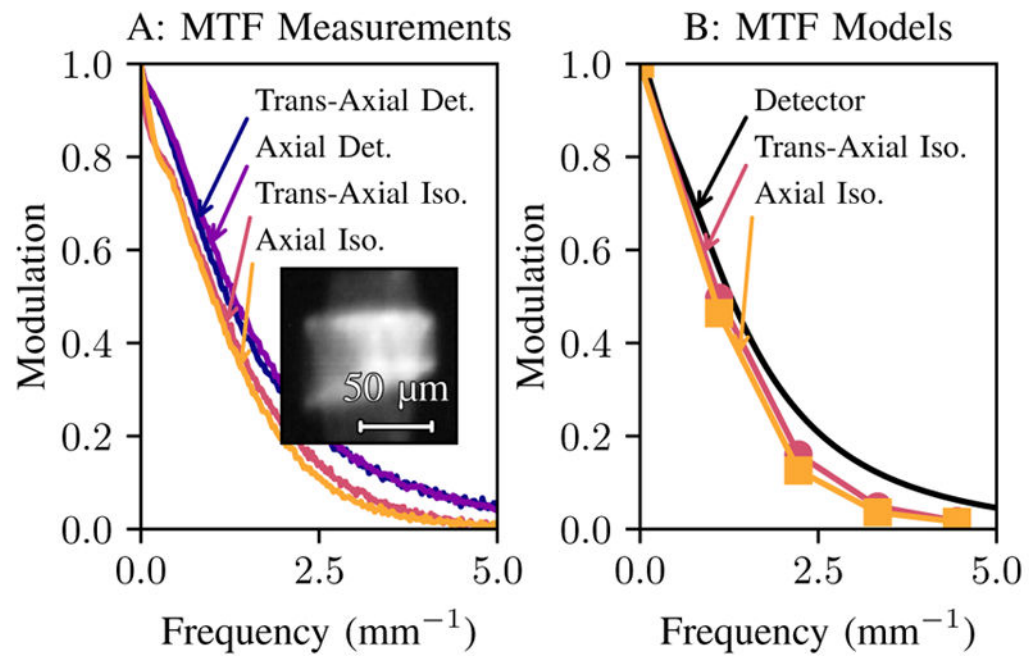
Fig. 2.
System Characterization Results. A: Measured axial and trans-axial MTF slices derived from tungsten edge responses. Inset: Pinhole image of the X-ray focal spot, resampled to match the PSF of the focal-spot blur experienced by an object at isocenter. B: MTF models. The detector model has the form given in (12). The isocenter models are slices of the MTF derived from the final PSF multiplied by the detector MTF model.
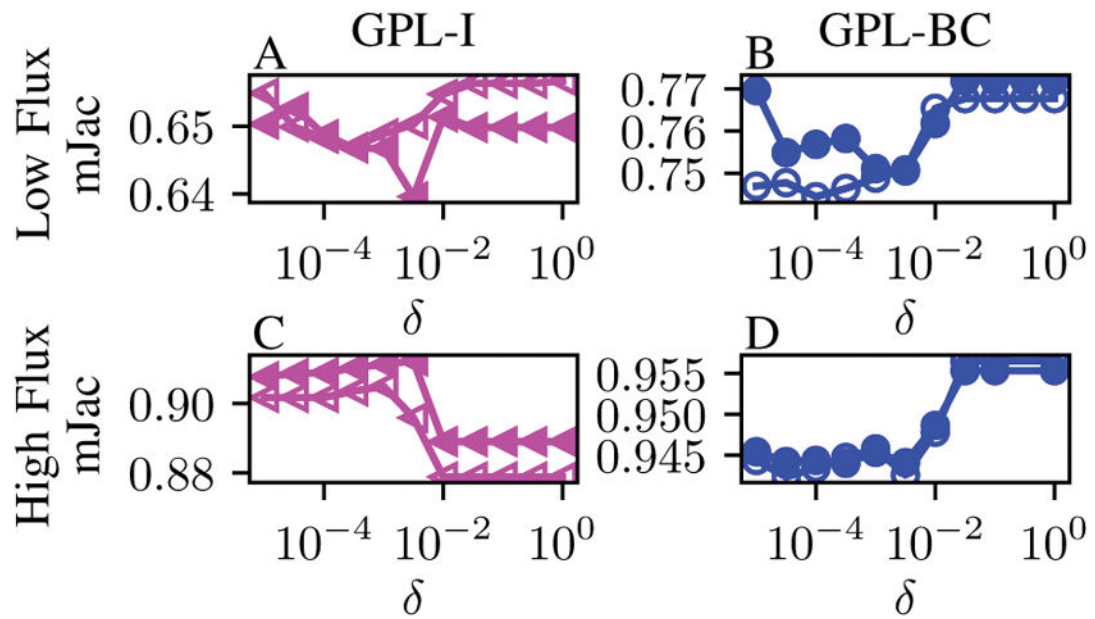
Fig. 3.
Parameter sweep results. Each point is the maximum mJac over β for a given δ, reconstruction method, and noise realization. The left column is GPL-I and the right column is GPL-BC. The top row is the low photon flux results and the bottom row is the high photon flux results.
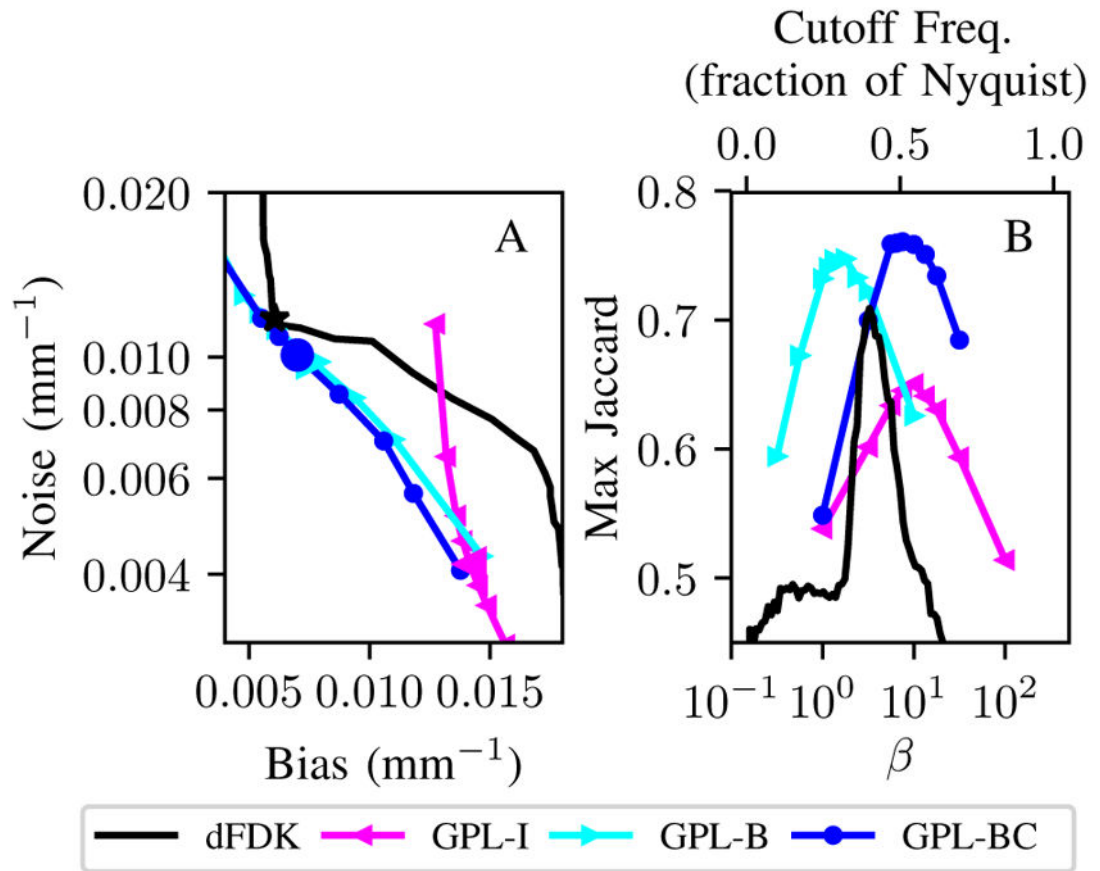
Fig. 4.
Bias/noise (A) and mJac (B) plots. The large markers in (A) correspond to the maximum mJacs in (B). The frequency cutoffs for the dFDK data in B (x-axis) are indicated at the top of the plot.
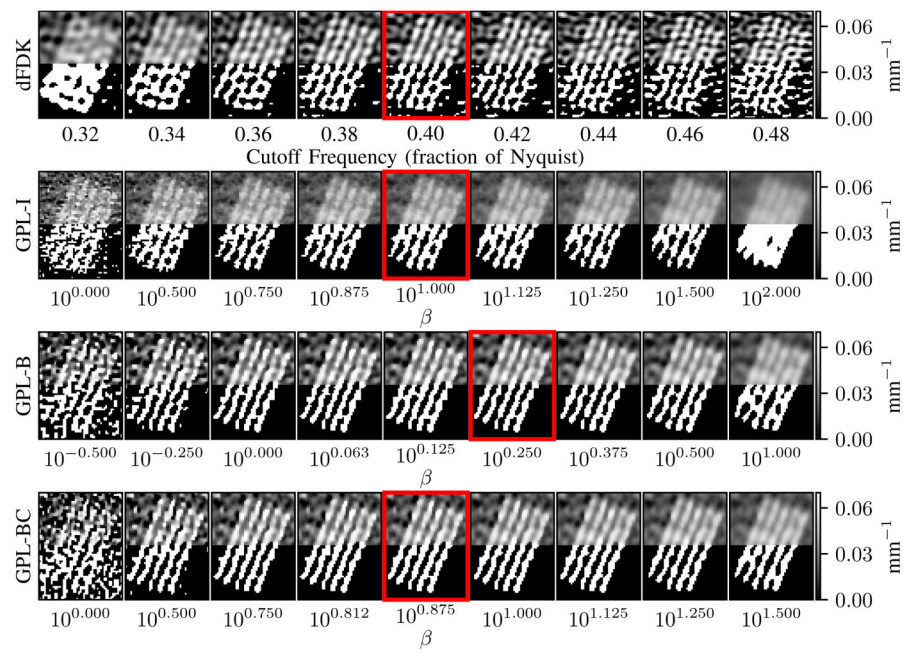
Fig. 5.
The center line pairs from the reconstructions in Fig. 4. Each row corresponds to a different reconstruction method. Note that different values of β were used for different MBIR methods. The reconstructions with the red border correspond to the ones with the maximum mJac in Fig. 4(B). The lower half of each image shows the best segmentation for that β/ cutoff (i.e., the one resulting in the maximum Jaccard index over threshold values).
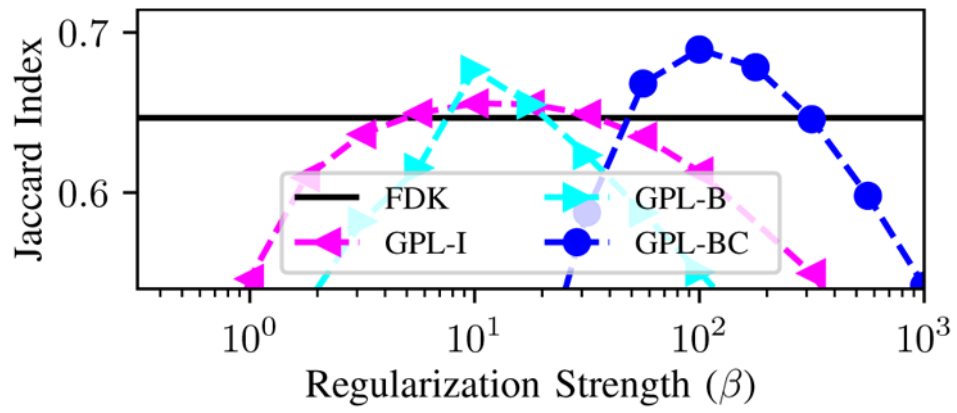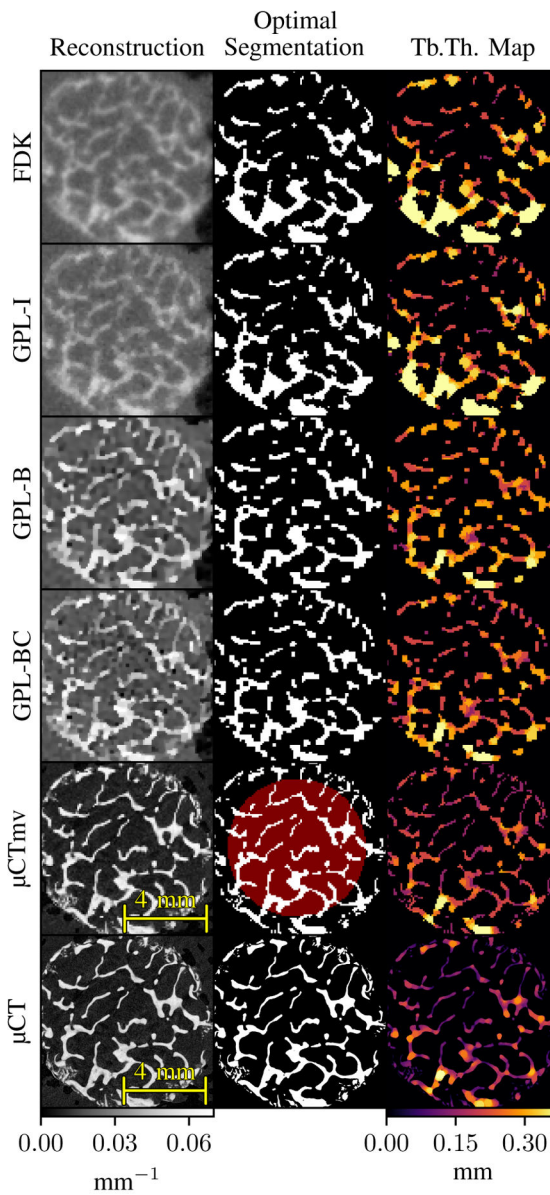
Fig. 6.
Maximum Jaccard (mJac) for each reconstruction method and regularization strength for the test bench-data.

Fig. 7.
Axial slice of trabecular bone reconstructions. Rows correspond to different reconstruction methods. The red background in the μCTmv segmentation image indicates a slice of the mask used for registration and metric calculation. Note the attenuation values of the μCT and μCTmv scans are arbitrary and do not correspond to the gray-level map on the bottom.
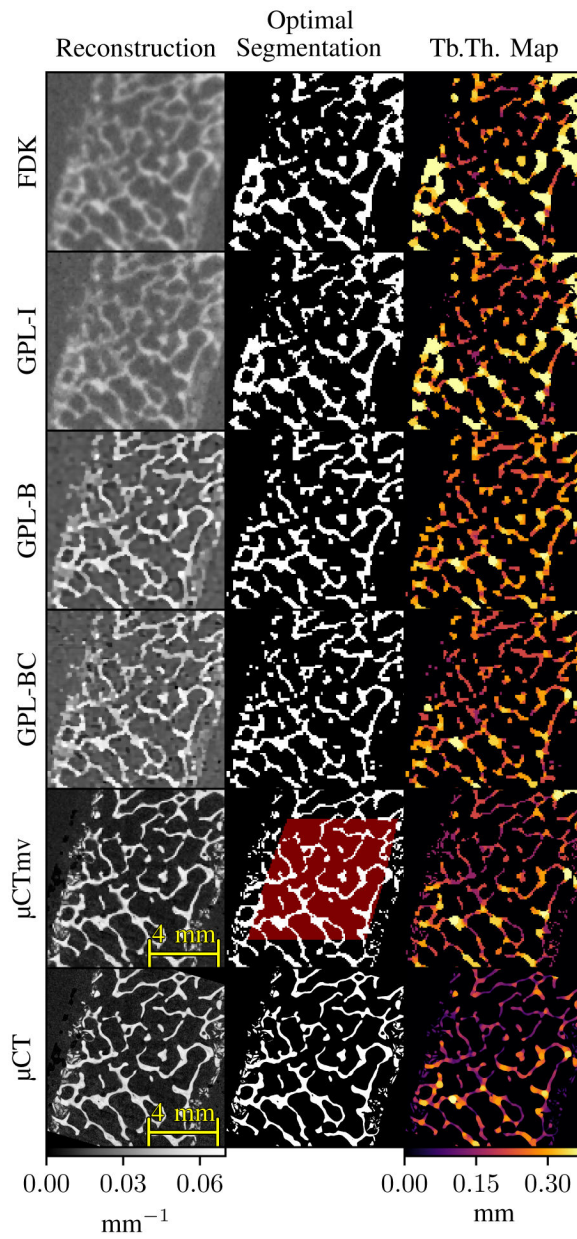
Fig. 8.

Trans-axial slice of trabecular bone reconstructions. μCT and μCTmv attenuation units are arbitrary.

TABLE I

Summary of Notation

Variable	Description	Nominal Value or Size
n_μ	Number of voxels	—
n_y	Number of measurements	—
$\boldsymbol{y}$	Measurements vector	n_y
$\mathbf{B}$	Gain/blur matrix	$n_y \times n_y$
$\mathbf{A}$	System matrix	$n_y \times n_\mu$
$\boldsymbol{\mu}$	Attenuation values vector	n_μ
$\mathbf{K}$	Measurement covariance	$n_y \times n_y$
$\mathbf{W}$	Weighting matrix ($\mathbf{K}^{-1}$)	$n_y \times n_y$
R	Regularizer/penalty function	$\mathbb{R}^{n_\mu} \to \mathbb{R}$
β	Penalty strength	—

TABLE II

Trabecular bone metric results.

	mean Tb.Th. (mm)	mean Tb.Sp. (mm)	BV/TV
FDK	0.335	0.860	0.214
GPL-I	0.309	0.824	0.216
GPL-B	0.271	0.785	0.224
GPL-BC	0.255	0.775	0.219
μCTmv	0.232	0.826	0.189
μCT	0.193	—	0.190